

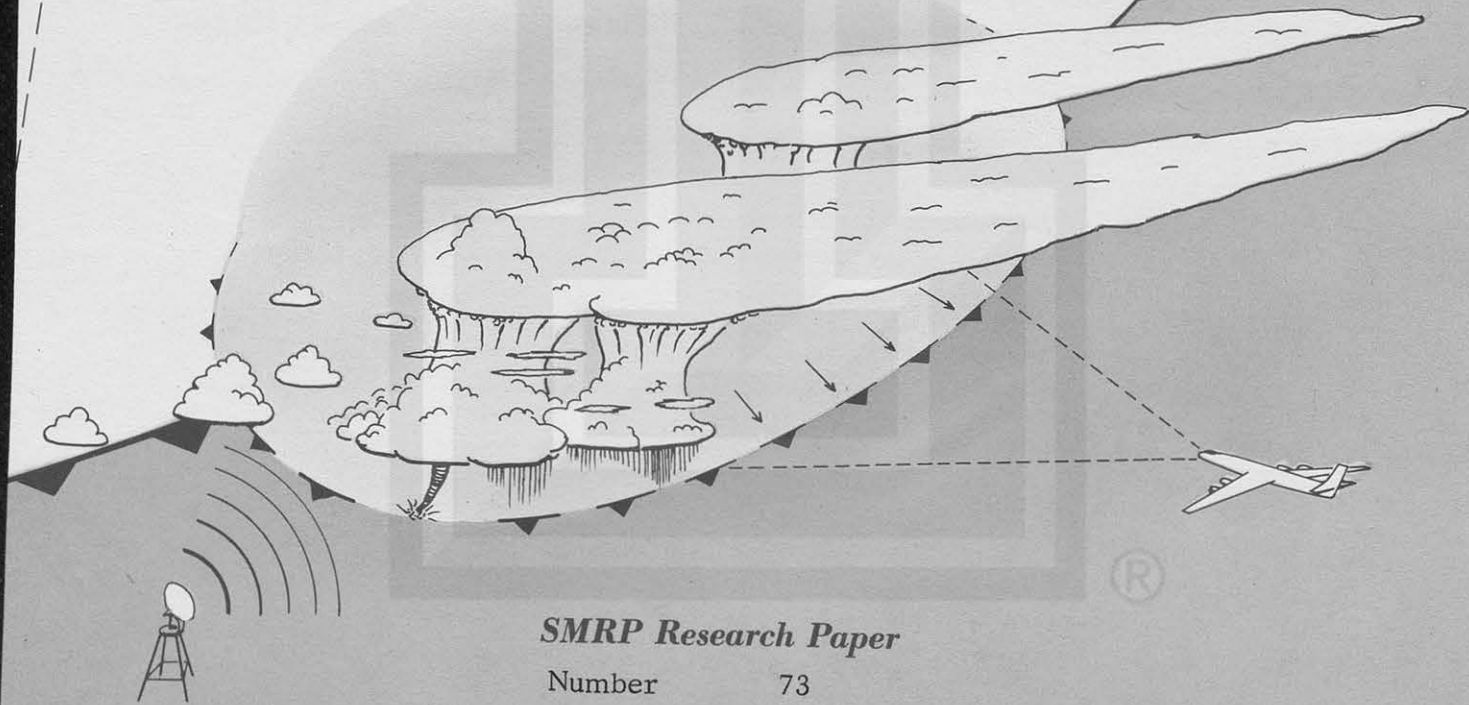
SATELLITE & MESOMETEOROLOGY RESEARCH PROJECT

Department of the Geophysical Sciences
The University of Chicago

ANGULAR DEPENDENCE OF REFLECTED SOLAR RADIATION FROM SAHARA MEASURED BY TIROS VII IN A TORQUING MANEUVER

by

Rene Mendez



SMRP Research Paper

Number 73

June 1968

MESOMETEOROLOGY PROJECT --- RESEARCH PAPERS

1. * Report on the Chicago Tornado of March 4, 1961 - Rodger A. Brown and Tetsuya Fujita
2. * Index to the NSSP Surface Network - Tetsuya Fujita
3. * Outline of a Technique for Precise Rectification of Satellite Cloud Photographs - Tetsuya Fujita
4. * Horizontal Structure of Mountain Winds - Henry A. Brown
5. * An Investigation of Developmental Processes of the Wake Depression Through Excess Pressure Analysis of Nocturnal Showers - Joseph L. Goldman
6. * Precipitation in the 1960 Flagstaff Mesometeorological Network - Kenneth A. Styber
7. ** On a Method of Single- and Dual-Image Photogrammetry of Panoramic Aerial Photographs - Tetsuya Fujita
8. A Review of Researches on Analytical Mesometeorology - Tetsuya Fujita
9. * Meteorological Interpretations of Convective Nephysystems Appearing in TIROS Cloud Photographs - Tetsuya Fujita, Toshimitsu Ushijima, William A. Hass, and George T. Dellert, Jr.
10. * Study of the Development of Prefrontal Squall-Systems Using NSSP Network Data - Joseph L. Goldman
11. Analysis of Selected Aircraft Data from NSSP Operation, 1962 - Tetsuya Fujita
12. Study of a Long Condensation Trail Photographed by TIROS I - Toshimitsu Ushijima
13. A Technique for Precise Analysis of Satellite Data; Volume I - Photogrammetry (Published as MSL Report No. 14) - Tetsuya Fujita
14. Investigation of a Summer Jet Stream Using TIROS and Aerological Data - Kozo Ninomiya
15. Outline of a Theory and Examples for Precise Analysis of Satellite Radiation Data - Tetsuya Fujita
16. Preliminary Result of Analysis of the Cumulonimbus Cloud of April 21, 1961 - Tetsuya Fujita and James Arnold
17. A Technique for Precise Analysis of Satellite Photographs - Tetsuya Fujita
18. * Evaluation of Limb Darkening from TIROS III Radiation Data - S.H.H. Larsen, Tetsuya Fujita, and W.L. Fletcher
19. Synoptic Interpretation of TIROS III Measurements of Infrared Radiation - Finn Pedersen and Tetsuya Fujita
20. * TIROS III Measurements of Terrestrial Radiation and Reflected and Scattered Solar Radiation - S.H.H. Larsen, Tetsuya Fujita, and W.L. Fletcher
21. On the Low-level Structure of a Squall Line - Henry A. Brown
22. * Thunderstorms and the Low-level Jet - William D. Bonner
23. * The Mesoanalysis of an Organized Convective System - Henry A. Brown
24. Preliminary Radar and Photogrammetric Study of the Illinois Tornadoes of April 17 and 22, 1963 - Joseph L. Goldman and Tetsuya Fujita
25. Use of TIROS Pictures for Studies of the Internal Structure of Tropical Storms - Tetsuya Fujita with Rectified Pictures from TIROS I Orbit 125, R/O 128 - Toshimitsu Ushijima
26. An Experiment in the Determination of Geostrophic and Isalobaric Winds from NSSP Pressure Data - William Bonner
27. Proposed Mechanism of Hook Echo Formation - Tetsuya Fujita with a Preliminary Mesosynoptic Analysis of Tornado Cyclone Case of May 26, 1963 - Tetsuya Fujita and Robbi Stuhmer
28. The Decaying Stage of Hurricane Anna of July 1961 as Portrayed by TIROS Cloud Photographs and Infrared Radiation from the Top of the Storm - Tetsuya Fujita and James Arnold
29. A Technique for Precise Analysis of Satellite Data, Volume II - Radiation Analysis, Section 6. Fixed-Position Scanning - Tetsuya Fujita
30. Evaluation of Errors in the Graphical Rectification of Satellite Photographs - Tetsuya Fujita
31. Tables of Scan Nadir and Horizontal Angles - William D. Bonner
32. A Simplified Grid Technique for Determining Scan Lines Generated by the TIROS Scanning Radiometer - James E. Arnold
33. A Study of Cumulus Clouds over the Flagstaff Research Network with the Use of U-2 Photographs - Dorothy L. Bradbury and Tetsuya Fujita
34. The Scanning Printer and Its Application to Detailed Analysis of Satellite Radiation Data - Tetsuya Fujita
35. Synoptic Study of Cold Air Outbreak over the Mediterranean using Satellite Photographs and Radiation Data - Aasmund Rabbe and Tetsuya Fujita
36. Accurate Calibration of Doppler Winds for their use in the Computation of Mesoscale Wind Fields - Tetsuya Fujita
37. Proposed Operation of Instrumented Aircraft for Research on Moisture Fronts and Wake Depressions - Tetsuya Fujita and Dorothy L. Bradbury
38. Statistical and Kinematical Properties of the Low-level Jet Stream - William D. Bonner
39. The Illinois Tornadoes of 17 and 22 April 1963 - Joseph L. Goldman
40. Resolution of the Nimbus High Resolution Infrared Radiometer - Tetsuya Fujita and William R. Bandeen
41. On the Determination of the Exchange Coefficients in Convective Clouds - Rodger A. Brown

- * Out of Print
 ** To be published

(Continued on back cover)

SATELLITE AND MESOMETEOROLOGY RESEARCH PROJECT

Department of the Geophysical Sciences

The University of Chicago

ANGULAR DEPENDENCE OF REFLECTED SOLAR RADIATION FROM SAHARA
MEASURED BY TIROS VII IN A TORQUING MANEUVER

by

Rene Mendez

SMRP Research Paper No. 73

June 1968



The research reported in this paper has been sponsored by the National Aeronautics and Space Administration, under Grant NASA NsG 333.

ANGULAR DEPENDENCE OF REFLECTED SOLAR RADIATION FROM SAHARA MEASURED BY TIROS VII IN A TORQUING MANEUVER¹

by

Rene Mendez

ABSTRACT

Statistical analyses have been made using observations of back-scattered radiation recorded by Channel 3 (0.2 to 6.0 microns) of the TIROS VII radiometer, as it passed over the Sahara Desert. Three orbits have been selected for this study.

In order that the results be consistent the areas involved were classified and labeled according to the terrain. A composite map of the area was then constructed from Gemini XI pictures and Nimbus I AVCS pictures.

Both closed mode scanning and alternating mode scanning have been used in order to obtain reflectance values from the ground at different angles of view. The following parameters have been considered: 1) type of ground surface; 2) scattering angle; 3) satellite zenith angle; 4) solar zenith angle; 5) azimuth of the TSP at the scan point; 6) azimuth of the sun at the scan point; and 7) relative azimuth. The results show a non-isotropic reflection pattern with maxima of scattering at low and high scattering angles, and at close to 0 and 180 deg relative azimuth. A minimum is found at about 125 deg of scattering angle and at close to 90 deg relative azimuth. The anisotropy is generally greater at satellite zenith angles and solar zenith angles greater than 45 deg.

1. Introduction

In order to have a better understanding of the world's weather processes, it is essential that more knowledge be gained about the heat budget of the earth. The earth's heat balance can be expressed as the difference between the incident solar energy and the outgoing radiant energy, the latter being the sum of the reflected solar radiation and the emitted thermal radiation.

¹The research reported in this paper has been sponsored by the National Aeronautics and Space Administration, under Grant NASA NsG 333.

Measurements of the reflected and scattered solar radiation are best when measured from the outside of the earth-atmosphere. This became possible with the development of satellites. Since in our case study the satellite is scanning quasi-homogeneous surfaces at different angles of view, the angular distribution of reflectance has been determined, thus a complete scattering pattern was obtained.

Ruff, et al., (1967) made a study of the patterns of reflection of solar radiation from clouds as a function of the zenith and azimuth angles, using statistical analysis of observations from TIROS IV visible radiation Channel 5 (0.55 to 0.75 microns).

The field of reflected filtered adjusted intensities over the hemisphere was determined for various ranges of solar zenith angles, and evidence of a generally non-isotropic reflection pattern was shown. The anisotropy was found to be greatest for large solar zenith angles. High intensity values were found for azimuth angles close to 180 deg from the sun and at large zenith angles. Bartman (1967) carried out a study of the reflected solar radiation with data obtained by radiometers flown on a series of high altitude balloon flights. A diagram of bidirectional reflectance as a function of scattering angle was constructed from data obtained while a balloon was flying over a stratocumulus cloud layer. A non-isotropic distribution of reflectance is clearly seen. Also, data obtained from another flight under clear skies over terrain 25-90% covered with wind-blown snow were plotted on a bidirectional reflectance diagram, with polar coordinate system of zenith angles versus azimuths from the sun. Results show high values of reflectance, on or close to 0-180 deg azimuths, and at large zenith angles. The departure from isotropy becomes greatest at large solar zenith angles.

Since both of these earlier studies were concerned with angular reflection from clouds or snow-covered surfaces, it was decided a similar study be made over homogeneous terrain under clear sky conditions. Therefore, the North African desert was selected as the area for this study since large areas of quasi-homogeneous terrain are found there.

Three orbits between 15 February and 27 February 1965 have been selected for this study. On Orbit 8975 R/O 8976, 15 February 1965, only the floor sensor data were available. During the period 15-22 February a torquing maneuver of the spin vector of about 105 deg was accomplished. This maneuver made it possible for daytime wall sensor measurements to be obtained. Thus on Orbits 9106 R/O 9107, 24 February, and 9150 R/O 9151, 27 February 1965, data were obtained from both wall and floor sensors.

2. Parameterization of the Sahara

For the purpose of mapping the terrain over North Africa, a number of AVCS pictures taken by Nimbus I as it passed over this area on cloud-free days were selected. These

were gridded accurately at 1 deg latitude-longitude intervals by matching features found on geographical and topographical maps. Figure 1 is one of the AVCS pictures with its superimposed grid. These were supplemented by pictures taken during the orbits of Gemini XI over the same area. In a like manner a 1 deg latitude-longitude grid was made for each of the Gemini pictures. Figure 2 is one of these pictures with its superimposed grid. As can be seen, the area covered by one Gemini picture is much larger than that covered by a Nimbus AVCS picture and has a higher resolution, thus showing more details. On both pictures the drifting or drifted sand (light areas) and bare rock (dark areas) are readily identifiable.

Using the AVCS and Gemini pictures a composite pseudo-geological chart of an area of North Africa between 18 to 34 deg N and 16 and 36 deg E was constructed. This map, shown in Fig. 3, separates the terrain into rock, mixed soil, and sand. In order to make it possible to compare reflection patterns from homogeneous surfaces, numbers were assigned to each of the surfaces, such as 0, 1, 3, and 5 to sea, rock, mixed soil, and sand, respectively, with the numbers 2 and 4 to varying degrees of mixed soil. Each one degree square was assigned a number between 0 and 5 corresponding to the type of terrain. The sum of four adjacent squares was plotted at the intersection of the grid lines and this value will henceforth be referred to as the ground parameter G . Figure 4 shows the distribution of the values assigned to the 1 deg squares and the G -values. When Fig. 4 is superimposed on Fig. 3, the following characteristics of the terrain are obtained: $G=0$, obviously represents the sea surface; $G=4 - 9$, indicates areas covered by rocks; $G=10 - 15$, shows predominantly mixed soil; and $G=16 - 20$, corresponds to areas covered mostly by sand. Since the purpose of this study is to determine the angular dependence of reflected solar radiation, the areas with G values between 16 and 20 became our fundamental concern as they represent the most homogeneous terrain to be expected. The satellite zenith angles of data involved were less than 50 deg, thus a ground parameter of $G=16 - 20$ would indicate scan spots predominantly filled by sand.

3. Measured Reflectance and the Ground Parameter

Radiation measurements from Channel 3 were obtained by the Scanning Printer (Fujita 1964) from analog traces of the five channel medium resolution scanning radiometer of TIROS VII. A sigma-t chart, in which coded radiation values printed along parallel lines representing successive scan lines, was produced. This chart is shown in Fig. 5A. The observations correspond to the complementary scans, floor sensor of Orbit 8975 R/O 8976, during a period of approximately five minutes. The data were obtained prior to the

torquing maneuver. Coordinates of latitudes and longitudes have been superimposed. It may be observed that the grid lines become parallel on the left side of the chart. This is the result of a closed mode scanning at the scan boundary. An analysis of the chart in c.p.s. units (cycles per second) is shown in Fig. 5B. With reference to this map analysis, the following features may be pointed out: higher values of reflected solar radiation are observed over the areas covered by sand; the low values appearing on the upper-left corner represent the high elevation area of "El Haruj el Aswald"; the circled low of 10 c.p.s. at the center of the map corresponds to "Jeb Uweinat" (elevation 1892 m); the Mediterranean coast line may be clearly identified. The encircled extreme high values of reflected solar radiation found on the right side of the map along the line of minimum scattering angle are "sun-spikes" which will be discussed later.

Computation of Reflectance

The incoming effective solar radiation upon a horizontal surface is represented by

$$\bar{W}^* \cos \zeta^*$$

in which \bar{W}^* is the effective solar constant in watts meter⁻², and ζ^* is the solar zenith angle. The effective reflectance, \bar{R} , reduced from one particular direction of observation by a satellite is obtained from

$$\bar{R} = \frac{\bar{W}}{\bar{W}^* \cos \zeta^*} \quad (1)$$

in which \bar{W} is the effective radiant emittance in watts meter⁻².

Under the assumption of isotropic radiation at the source and no attenuation between the source and the satellite, the effective radiance \bar{N} is given by

$$\bar{N} = \frac{\bar{W}}{\pi}$$

if the reflecting source is a perfectly diffuse reflector. The earth's surface is not a perfectly diffuse reflector, and in order to obtain an apparent reflectance or albedo, A , the effective reflectance obtained must be integrated in all directions. If M represents the outgoing effective reflected solar radiation in the upper atmosphere,

$$M = \int_{\alpha=0}^{2\pi} \int_{\zeta=0}^{\frac{\pi}{2}} \frac{\bar{W}}{\pi} \cos \zeta^\circ \sin \zeta^\circ d\zeta^\circ d\alpha$$

then albedo,

$$A = \frac{M}{\overline{W}^* \cos \zeta^*}$$

or

$$A = \frac{\frac{1}{\pi} \int_0^{2\pi} \int_0^{\frac{\pi}{2}} \overline{W} \cos \zeta^\circ \sin \zeta^\circ d\zeta^\circ d\alpha}{\overline{W}^* \cos \zeta^*}$$

therefore,

$$A = \frac{1}{\pi} \int_0^{2\pi} \int_0^{\frac{\pi}{2}} \overline{R} \cos \zeta^\circ \sin \zeta^\circ d\zeta^\circ d\alpha \quad (2)$$

where

$$\overline{R} = f(\alpha^{\text{TSP}}, \alpha^*, \zeta^*, \zeta^\circ, \psi, \Delta\alpha, G)$$

in which α^{TSP} is the azimuth of the TSP (Terrestrial Subsatellite Point) measured at the scan point from north in a clockwise direction, α^* is the azimuth of the TSS (Terrestrial Subsolar Point) measured at the scan point from north in a clockwise direction, ζ^* is the solar zenith angle, ζ° is the satellite zenith angle, ψ is the scattering angle, $\Delta\alpha$ is the relative azimuth, and G is the ground parameter.

From the data shown in Figs. 5A and 5B, calculations of the effective reflectance, \overline{R} , in percent were made, and a reflectance map was constructed, as shown in Fig. 6, scan lines on the minute were included. The high reflectance values corresponding to the areas covered by sand and the low reflectance values corresponding to the Mediterranean Sea, the Red Sea, and the areas covered by rock can be clearly observed.

The values of effective reflectance, \overline{R} , in percent mentioned above, together with the values obtained from observations of the initial scans of Orbit 8975 R/O 8976, and the values obtained from observations by the wall sensors of Orbits 9106 R/O 9107 and 9150 R/O 9151 after the torquing, were plotted as a function of the ground parameter. Then, mean curves of reflectance were drawn, one corresponding to the wall sensor and another corresponding to the floor sensor, as shown in Fig. 7. It may be easily seen that the wall sensor reflectance curve is higher than the floor sensor reflectance curve. This may be attributed to AOD (assymetrical optical degradation) in conjunction with the geometry of the several parameters involved in the measured reflected solar radiation. However, as mentioned earlier, this study is not intended to determine the exact magnitude of the reflectance. Since our purpose is to determine the ability of the satellite measurements to detect an anisotropic distribution of reflectance over a cloudless area, this difference does not affect our problem. Figure 7 shows clearly the non-homogeneity of the earth's reflected solar radiation.

4. Computations of Satellite Zenith Angles, Scattering Angles, and Relative Azimuths

The satellite zenith angle at the scan point, ζ° , is the vertical angle between the local vertical of TSC (Terrestrial Scan Point) and the radiometer axis and

$$\zeta^\circ = f(\eta_0, \bar{R}_e, H)$$

in which η_0 is the nadir angle of the scan point, \bar{R}_e the mean radius of the earth, and the height of the satellite. Thus,

$$\zeta^\circ = \frac{H + \bar{R}_e}{\bar{R}} \sin \eta_0$$

The scattering, ψ is the angle between the incident and the outgoing beam and

$$\psi = f(\zeta^\circ, \zeta^*, \Delta\alpha)$$

The relationship between the scattering angle, the satellite zenith angle, and the relative azimuth, is expressed by

$$\cos \psi = (\cos \zeta^\circ \cos \zeta^*) + (\sin \zeta^\circ \sin \zeta^* \cos \Delta\alpha) \quad (4)$$

where the relative azimuth, $\Delta\alpha$ is the difference between the azimuth of TSS, α^{TSS} and the azimuth of TSP, α^{TSP} .

Figure 8 shows the analysis of the data recorded on Orbit 8975 R/O 8976 from the complementary scans of the floor sensor. Isolines are drawn for the scan lines every 60 seconds, the scattering angles for every 10 deg, and the satellite zenith angles also for every 10 deg. The geometry of the relative azimuth is indicated by the solid and broken lines with arrowheads on scan lines 34 and 35.

On the map of effective reflectance, \bar{R} , (Fig. 6), isolines of solar zenith angles (45 deg, 50 deg, 55 deg) and the isoline of minimum scattering angle (heavy line) have been included as shown in Fig. 9. Those values encircled along the minimum scattering line are the effective reflectance, \bar{R} in percent obtained during the sun spikes. The sun spikes occurred when direct sun rays were being intersected by the wall sensor.

5. Change in Reflectance as a Function of the Satellite Zenith Angles

The values of reflectance obtained in order to construct (Fig. 6) were plotted as a

function of the satellite zenith angles over the areas where the ground parameter was $G=16 - 20$. Then a mean reflectance curve was drawn, as shown in Fig. 10. It may be easily observed that higher values of reflectance are found when the satellite zenith angles increase.

6. Change in Reflectance as a Function of Scattering Angles and Relative Azimuths

Using the same data as above, the values of reflectance were plotted as a function of the scattering angles over the areas where the ground parameter was $G=10 - 15$ (mixed soil) and $G=16 - 20$ (sand). Figure 11 shows the distribution of reflectance for the two types of terrain. The non-isotropic nature of the earth's reflectance is clearly seen. One maximum of reflectance is found in the forward scattering direction and a second maximum is found in the backward scattering direction. A minimum value of reflectance is found at about 125 deg of scattering angle.

The same data were also plotted in a diagram of satellite zenith angles versus azimuthal angles. Then, mean values of reflectance were plotted on a reflection diagram as shown in Fig. 12. Once again, a non-isotropic pattern of reflectance is observed. Maxima are found at close to 0 and 180 deg relative azimuth. A minimum is found at 90 deg relative azimuth. It may also be observed that reflectance is greatest at satellite zenith angles near 55 deg.

7. Satellite Spin Axis Nutation

"Sun spikes" occur when the gamma angle is equal or close to the inclination of radiometer axis (45 deg). In terrestrial coordinates the gamma angle is defined as the angle between TSA (Terrestrial Spin-Axis Point) and TSS (Terrestrial Subsolar Point). Under these conditions the wall sensor intersects the direct rays of the sun, and direct solar radiation is impinged upon the sensors through the wall side, once during each spin.

This was the case in Orbit 8960 R/O 8961, one of the orbits previously selected for our study, in which the gamma angle was 45.3 deg. However, Orbit 8975 R/O 8976, gamma angle 35.7 deg, the radiometer was recording "sun spikes" intermittently, along the line of minimum scattering angle. In order to investigate this case further, we proceeded to obtain from the analog traces the values of the reflected solar radiation for each spin at that particular point, for the entire period covered in our study. These values were plotted as a function of the spin, as shown in Fig. 13. It may be clearly observed that the satellite spin axis is wobbling, therefore, intersecting the direct rays of the sun

through the wall sensor every other spin. The cycle appeared to show 10 spins under this effect followed by 3 spins free of it. The geometry of the wobbling is also shown in Fig. 13. Computations showed a satellite spin axis oscillation around $180^{\pm 11}$ deg.

8. Conclusions

The above study has been carried out with the purpose of determining the ability of satellite measurements to detect an anisotropic distribution of reflectance over a cloudless area.

Results show a clear evidence of a non-isotropic reflectance with a maximum in the forward scattering direction and another maximum in the backward scattering direction. The first is greater than the second. Also, maxima of reflectance were found at close to 0 and 180 deg azimuth from the sun.

Satellite measurements also showed that the earth is a non-homogeneous reflector of the solar radiation.

ACKNOWLEDGEMENTS:

The author wishes to thank Miss Dorothy L. Bradbury for her help in preparing the manuscript.



REFERENCES

- Bartman, Fred L., 1967: The reflectance and scattering of solar radiation by the earth. Univ. of Michigan Tech. Rep. No. 05863-11-T, 1-124.
- Fujita, T., 1964: The scanning printer and its application to detailed analysis of satellite radiation data. SMRP Res. Paper No. 34, 29 pp.
- Ruff, I.R., S. Koffler, S. Fritz, and P. K. Rao, 1967: Angular distribution of solar radiation reflected from clouds as determined from TIROS IV radiometer measurements. ESSA Tech. Rep. No. NESC-38, 64 pp.



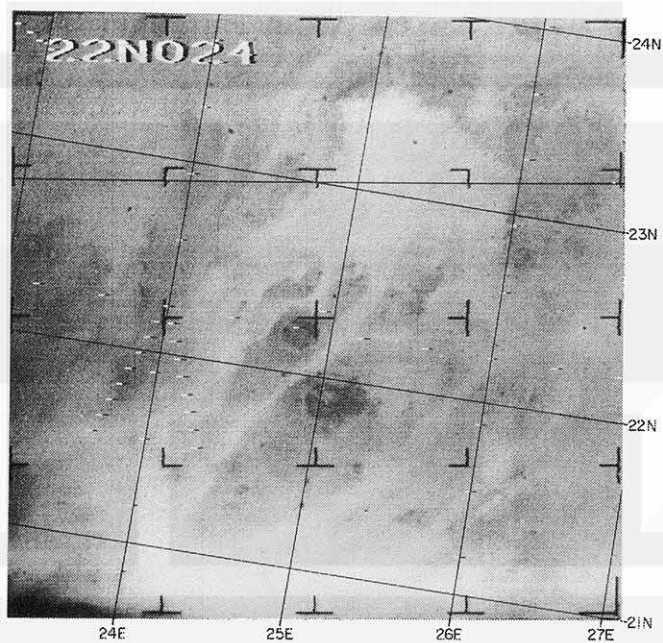


Fig. 1. AVCS picture of Nimbus I corresponding to Orbit 294, camera 2, 17 September 1964.

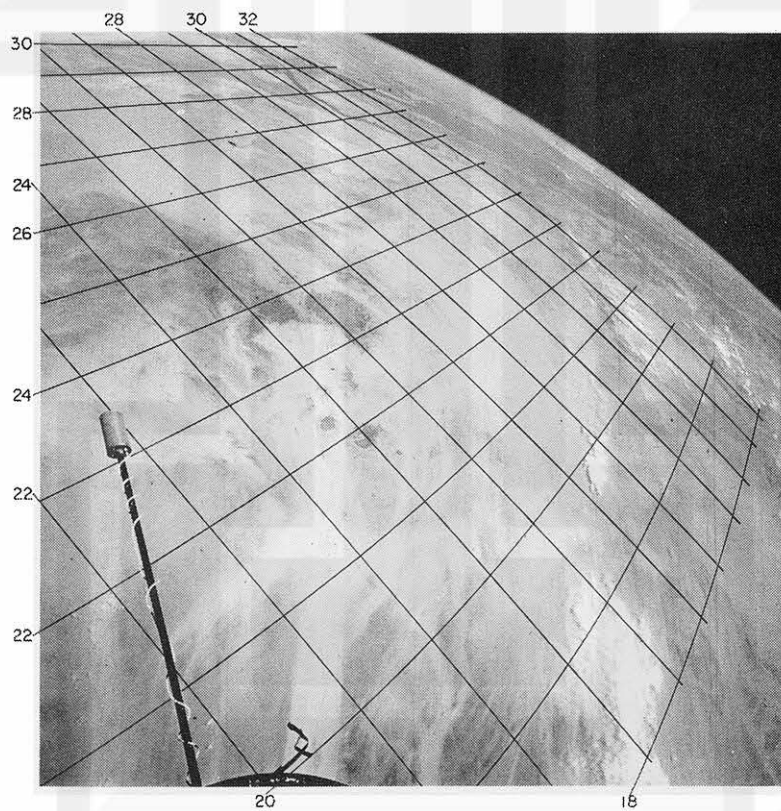


Fig. 2. Gemini XI picture.

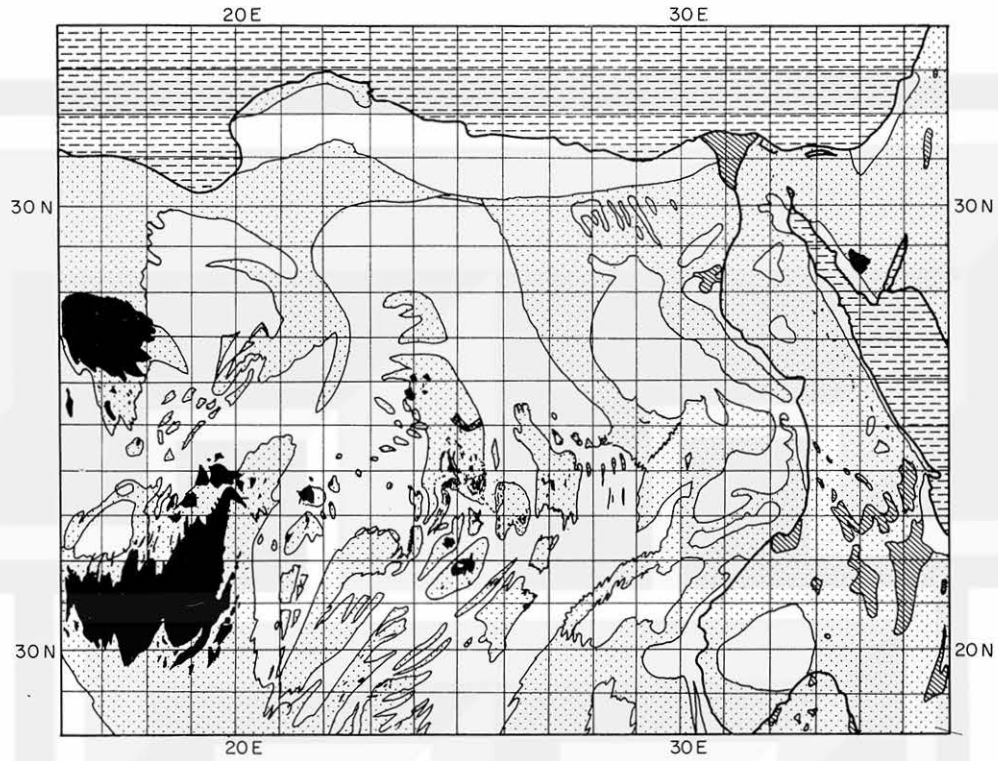


Fig. 3. Composite pseudo-geological map of North Africa, constructed from several Nimbus I AVCS pictures and Gemini XI pictures.

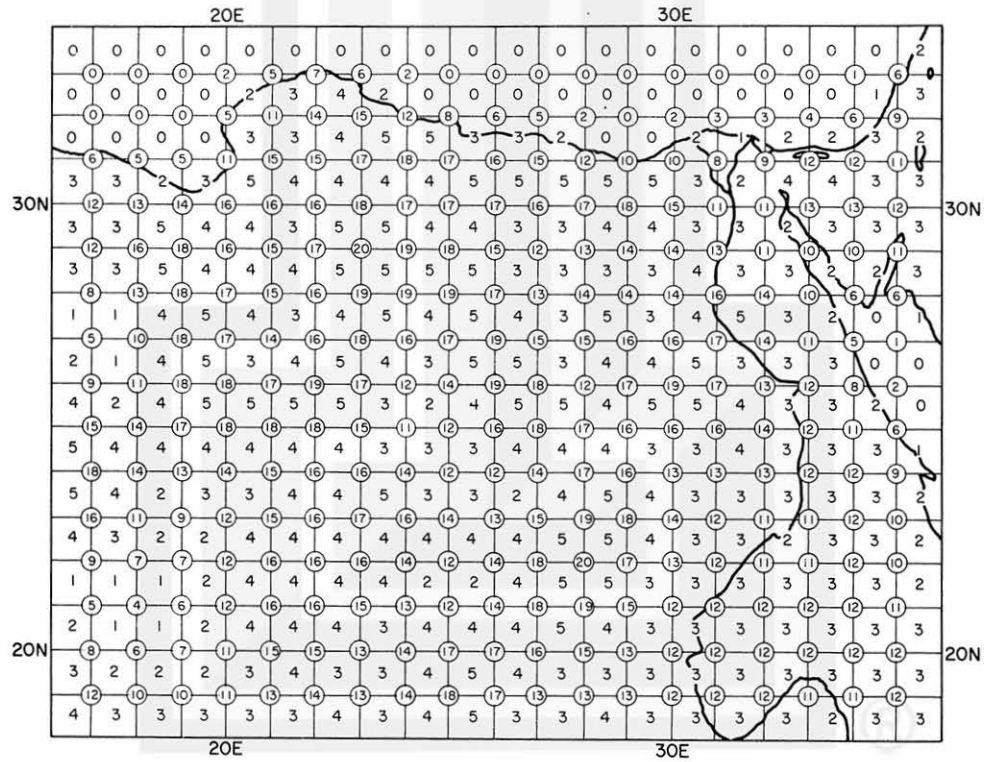


Fig. 4. Parameterization of the area of our study.

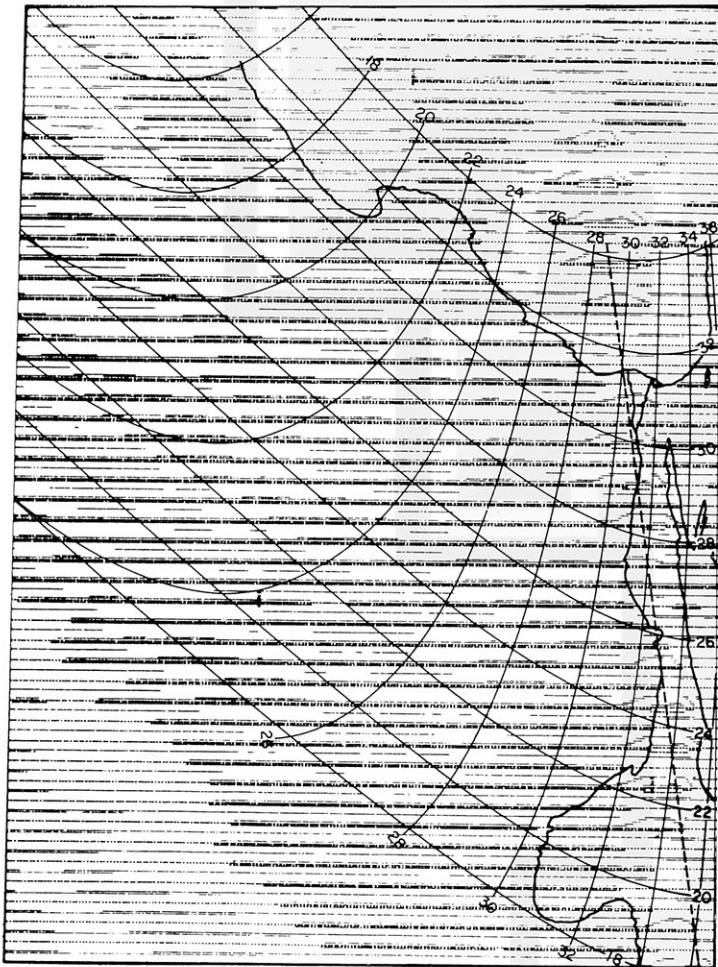


Fig. 5A. Sigma-t chart obtained from analog trace of Orbit 8975 R/O 8976, 15 February 1965, Channel 3, complementary scans, floor sensor, observations were obtained prior to the torquing maneuver.

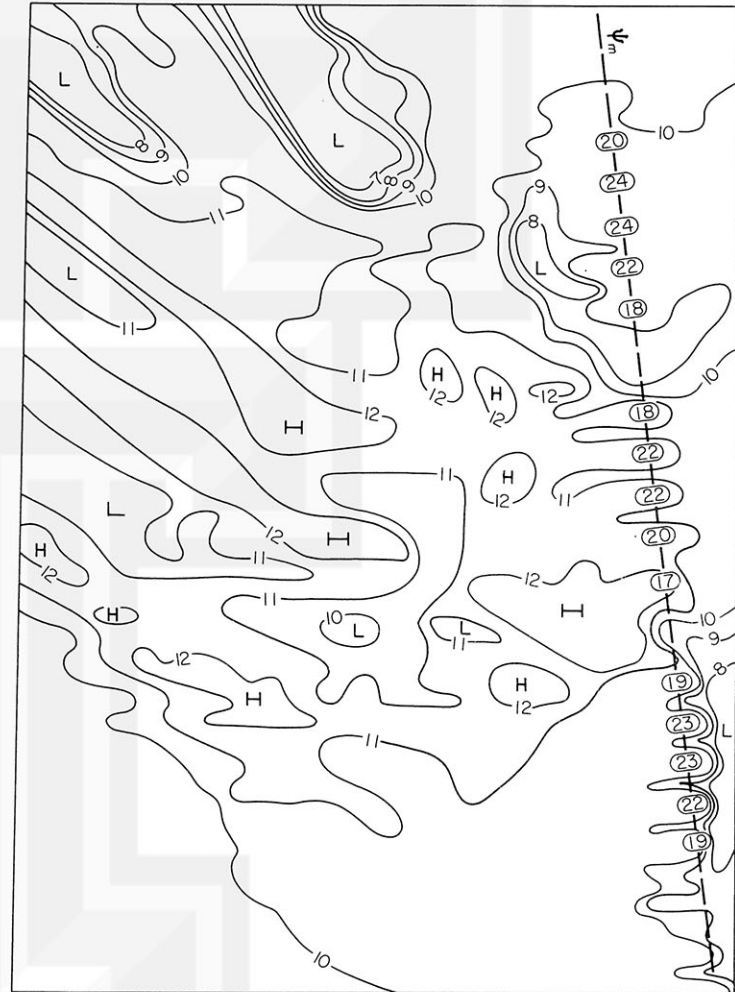


Fig. 5B. Analyzed map in c.p.s. units (cycles per second) of data shown in Fig. 5A.

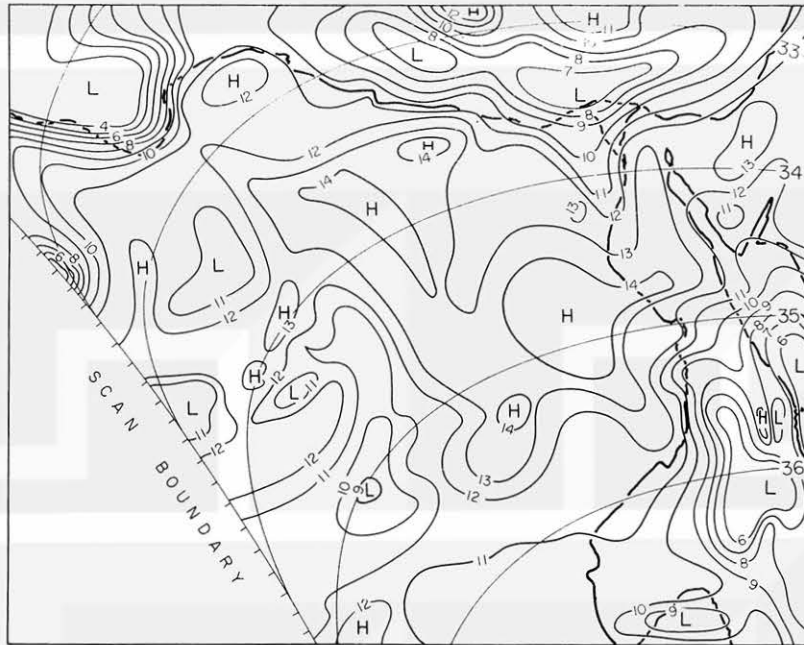


Fig. 6. Map of effective reflectance, \bar{R} , in percent obtained from data shown in Figs. 5A and 5B.

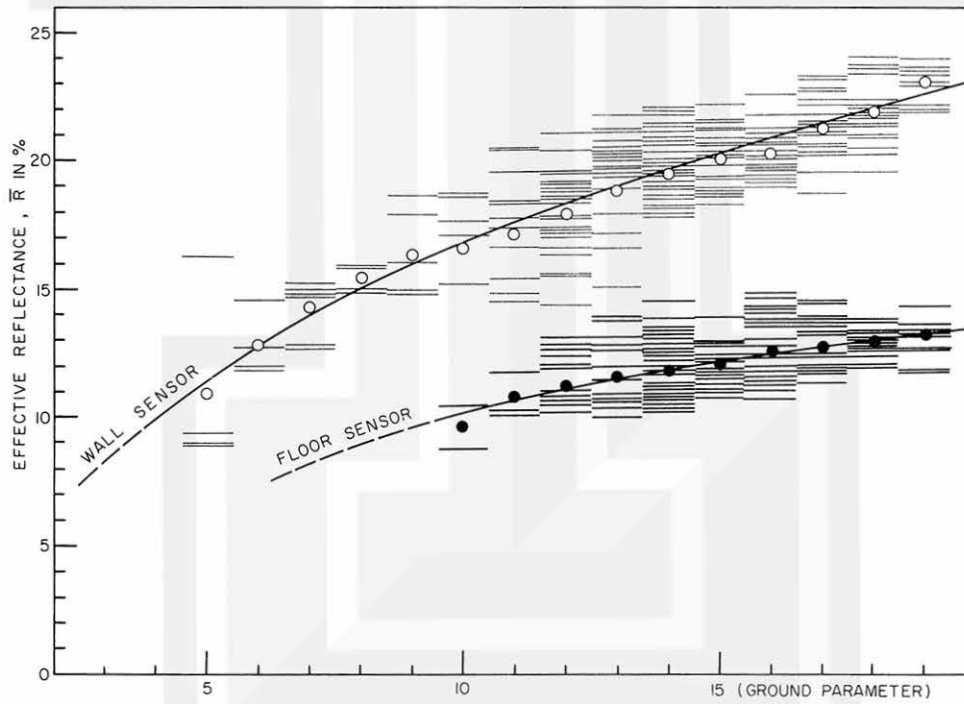


Fig. 7. Effective reflectance, \bar{R} , in percent as a function of the ground parameter.

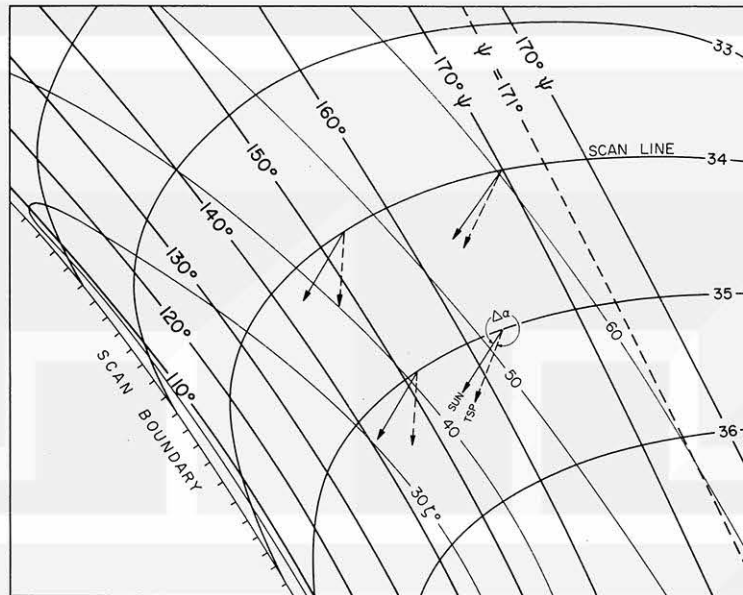


Fig. 8. Isolines of: scan lines every 60 seconds, scattering angles, ψ , every 10 deg, and satellite zenith angles, ζ° , also every 10 deg. The geometry of the relative $\Delta\alpha$, is shown on scan lines 34 and 35. Data correspond to Orbit 8975 R/O 8976, complementary scans, floor sensor, obtained prior to the torquing.

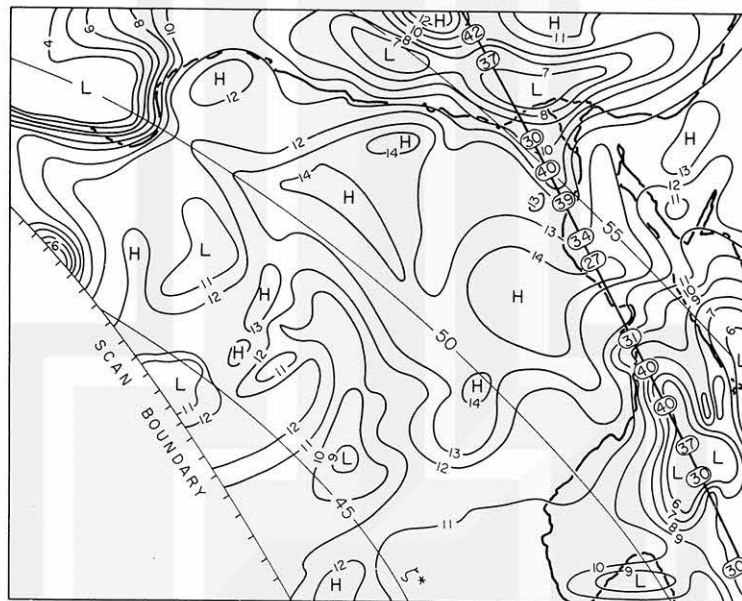


Fig. 9. Effective reflectance, \bar{R} , in percent shown in Fig. 6. Isolines of the solar zenith angles, ζ^* , and minimum scattering angle, ψ_m , have been included.

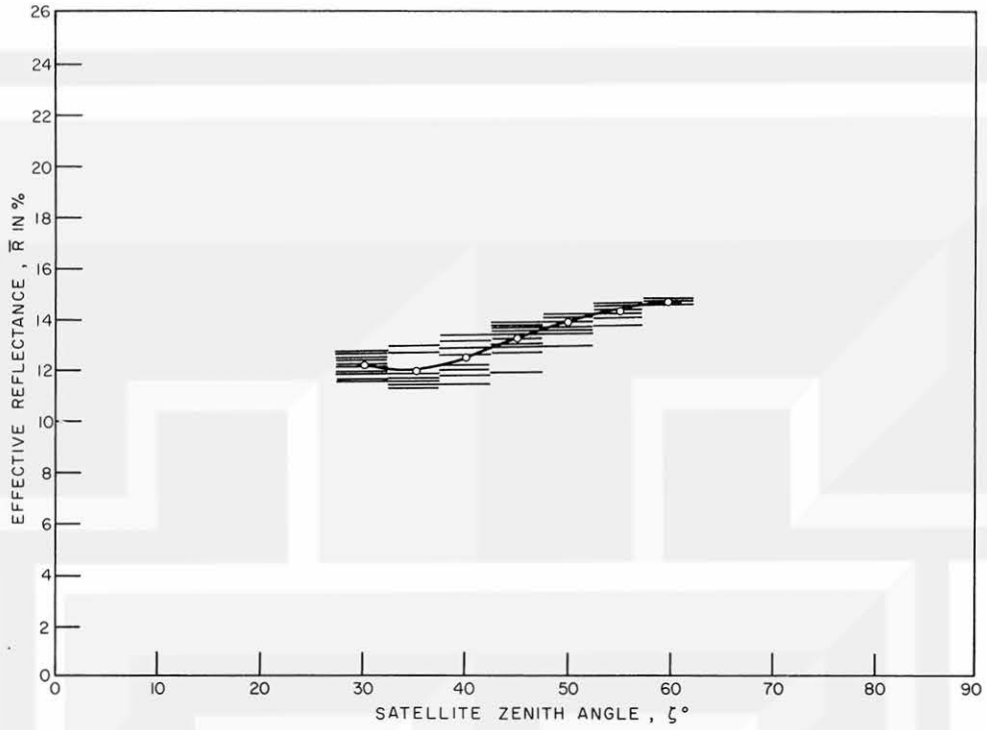


Fig. 10. Effective reflectance, \bar{R} , in percent as a function of the satellite zenith angles, ζ° .

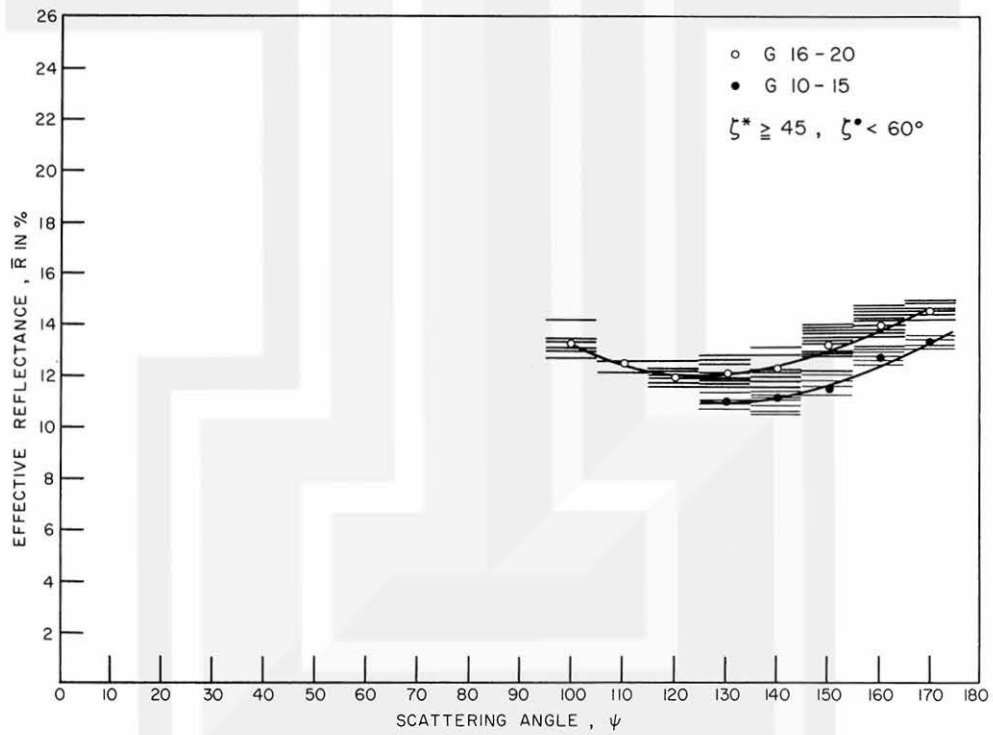


Fig. 11. Effective reflectance, \bar{R} , in percent as a function of the scattering angles, ψ .

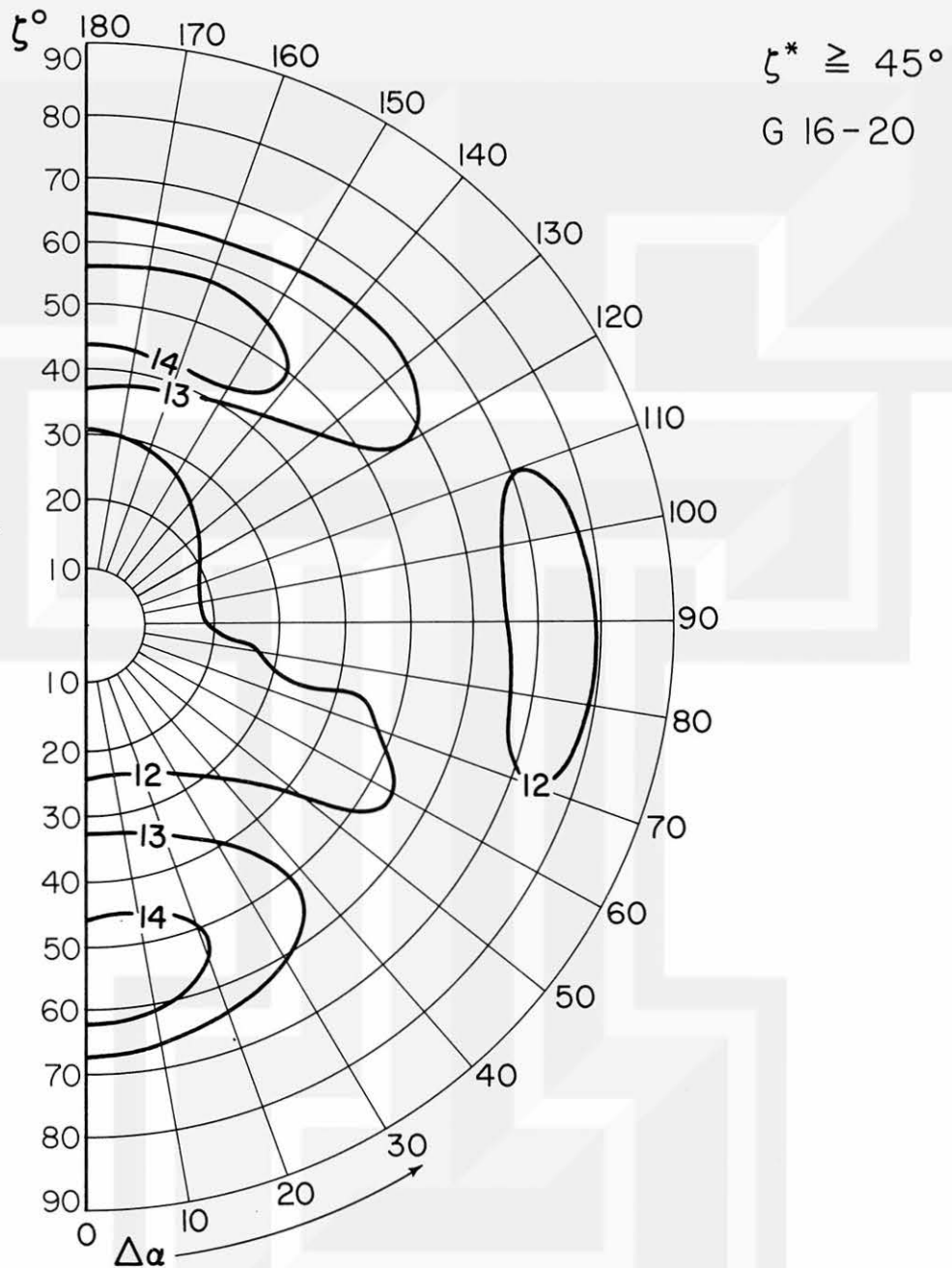


Fig. 12. Effective reflectance, \bar{R} , in percent as a function of the relative azimuth, $\Delta\alpha$.

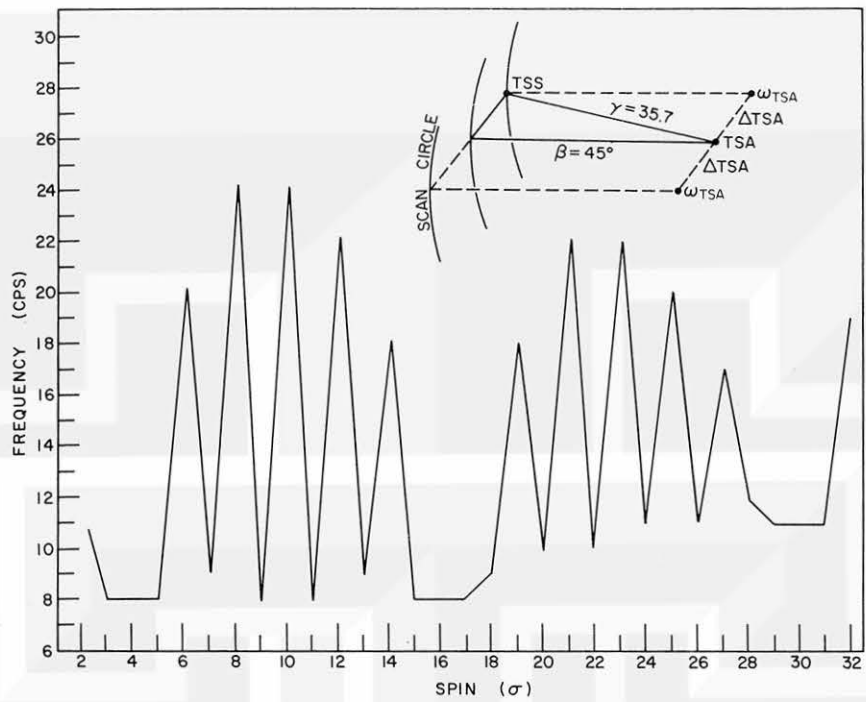


Fig. 13. Nutation of the spin axis on Orbit 8975 R/O 8976, data correspond to the complementary scans, floor sensor.

MESOMETEOROLOGY PROJECT - - - RESEARCH PAPERS

(Continued from front cover)

42. ^{*} A Study of Factors Contributing to Dissipation of Energy in a Developing Cumulonimbus -
Rodger A. Brown and Tetsuya Fujita
43. A Program for Computer Gridding of Satellite Photographs for Mesoscale Research -
William D. Bonner
44. Comparison of Grassland Surface Temperatures Measured by TIROS VII and
Airborne Radiometers under Clear Sky and Cirriform Cloud Conditions - Ronald
M. Reap
45. Death Valley Temperature Analysis Utilizing Nimbus I Infrared Data and Ground-
Based Measurements - Ronald M. Reap and Tetsuya Fujita
46. On the "Thunderstorm-High Controversy" - Rodger A. Brown
47. Application of Precise Fujita Method on Nimbus I Photo Gridding - Lt. Cmd.
Ruben Nasta
48. A Proposed Method of Estimating Cloud-top Temperature, Cloud Cover, and
Emissivity and Whiteness of Clouds from Short- and Long-wave Radiation Data
Obtained by TIROS Scanning Radiometers - T. Fujita and H. Grandoso
49. Aerial Survey of the Palm Sunday Tornadoes of April 11, 1965 - Tetsuya Fujita
50. Early Stage of Tornado Development as Revealed by Satellite Photographs -
Tetsuya Fujita
51. Features and Motions of Radar Echoes on Palm Sunday, 1965 - D. L. Bradbury
and Tetsuya Fujita
52. Stability and Differential Advection Associated with Tornado Development -
Tetsuya Fujita and Dorothy L. Bradbury
53. Estimated Wind Speeds of the Palm Sunday Tornadoes - Tetsuya Fujita
54. On the Determination of Exchange Coefficients: Part II - Rotating and Nonrotating
Convective Currents - Rodger A. Brown
55. Satellite Meteorological Study of Evaporation and Cloud Formation over the
Western Pacific under the Influence of the Winter Monsoon - K. Tsuchiya and
T. Fujita
56. A Proposed Mechanism of Snowstorm Mesojet over Japan under the Influence of
the Winter Monsoon - T. Fujita and K. Tsuchiya
57. Some Effects of Lake Michigan upon Squall Lines and Summertime Convection -
Walter A. Lyons
58. Angular Dependence of Reflection from Stratiform Clouds as Measured by TIROS IV
Scanning Radiometers - A. Rabbe
59. Use of Wet-beam Doppler Winds in the Determination of the Vertical Velocity
of Raindrops inside Hurricane Rainbands - T. Fujita, P. Black and A. Loesch
60. A Model of Typhoons Accompanied by Inner and Outer Rainbands - Tetsuya
Fujita, Tatsuo Izawa, Kazuo Watanabe, and Ichiro Imai

MESOMETEOROLOGY PROJECT - - - RESEARCH PAPERS

(Continued from inside back cover)

61. Three-Dimensional Growth Characteristics of an Orographic Thunderstorm System - Rodger A. Brown.
62. Split of a Thunderstorm into Anticyclonic and Cyclonic Storms and their Motion as Determined from Numerical Model Experiments - Tetsuya Fujita and Hector Grandoso.
63. Preliminary Investigation of Peripheral Subsidence Associated with Hurricane Outflow - Ronald M. Reap.
64. The Time Change of Cloud Features in Hurricane Anna, 1961, from the Easterly Wave Stage to Hurricane Dissipation - James E. Arnold.
65. Easterly Wave Activity over Africa and in the Atlantic with a Note on the Inter-tropical Convergence Zone during Early July 1961 - James E. Arnold.
66. Mesoscale Motions in Oceanic Stratus as Revealed by Satellite Data - Walter A. Lyons and Tetsuya Fujita.
67. Mesoscale Aspects of Orographic Influences on Flow and Precipitation Patterns - Tetsuya Fujita.
68. A Mesometeorological Study of a Subtropical Mesocyclone - Hidetoshi Arakawa, Kazuo Watanabe, Kiyoshi Tsuchiya, and Tetsuya Fujita.
69. Estimation of Tornado Wind Speed from Characteristic Ground Marks - Tetsuya Fujita, Dorothy L. Bradbury, and Peter G. Black.
70. Computation of Height and Velocity of Clouds from Dual, Whole-Sky, Time-Lapse Picture Sequences - Dorothy L. Bradbury and Tetsuya Fujita.
71. A Study of Mesoscale Cloud Motions Computed from ATS-I and Terrestrial Photographs - Tetsuya Fujita, Dorothy L. Bradbury, Clifford Murino, and Louis Hull.
72. Aerial Measurement of Radiation Temperatures over Mt. Fuji and Tokyo Areas and Their Application to the Determination of Ground- and Water-Surface Temperatures - Tetsuya Fujita, Gisela Baralt, and Kiyoshi Tsuchiya.

